Published in final edited form as:
IEEE Trans Biomed Circuits Syst. 2009 October ; 3(5): 339–347. doi:10.1109/TBCAS.2009.2025366.

Modeling and Optimization of Printed Spiral Coils in Air, Saline, and Muscle Tissue Environments

Uei-Ming Jow [Student Member, IEEE] and **Maysam Ghovanloo [Member, IEEE]**
GT-Bionics Lab, School of Electrical and Computer Engineering, Georgia Institute of Technology, Atlanta, GA 30308 USA

Abstract

Printed spiral coils (PSCs) are viable candidates for near-field wireless power transmission to the next generation of high-performance neuroprosthetic devices with extreme size constraints, which will target intraocular and intracranial spaces. Optimizing the PSC geometries to maximize the power transfer efficiency of the wireless link is imperative to reduce the size of the external energy source, heating of the tissue, and interference with other devices. Implantable devices need to be hermetically sealed in biocompatible materials and placed in a conductive environment with high permittivity (tissue), which can affect the PSC characteristics. We have constructed a detailed model that includes the effects of the surrounding environment on the PSC parasitic components and eventually on the power transfer efficiency. We have combined this model with an iterative design method that starts with a set of realistic design constraints and ends with the optimal PSC geometries. We applied our design methodology to optimize the wireless link of a 1-cm^2 implantable device example, operating at 13.56 MHz. Measurement results showed that optimized PSC pairs, coated with 0.3 mm of silicone, achieved 72.2%, 51.8%, and 30.8% efficiencies at a face-to-face relative distance of 10 mm in air, saline, and muscle, respectively. The PSC, which was optimized for air, could only bear 40.8% and 21.8% efficiencies in saline and muscle, respectively, showing that by including the PSC tissue environment in the design process the result can be more than a 9% improvement in the power transfer efficiency.

Keywords

Implantable microelectronic devices; inductive wireless links; neuroprostheses; power transmission efficiency; printed spiral coils (PSCs); telemetry

I. Introduction

COCHLEAR implants, spinal cord stimulators, infusion pumps, and artificial hearts are among an ever-growing number of implantable devices that are wirelessly powered across the skin barrier through a pair of inductively coupled coils [1]. A common requirement among these otherwise diverse biomedical devices is that their average power consumption is higher than what a battery, fitting within the anatomically available space for implantation, can provide.

Research is currently underway to develop a whole new group of implantable devices, such as retinal implants and intracranial brain-computer interfaces (BCI), with even stricter size

mgh@gatech.edu .
Color versions of one or more of the figures in this paper are available online at http://ieeexplore.ieee.org

constraints. These are expected to be placed inside the eyeball through a 5-mm incision or within the 1~3-mm epidural spacing between the outer surface of the brain and the skull [2], [3]. Therefore, the need for more efficient wireless power transmission from outside into the human body, with a much smaller footprint, is only expected to grow.

Fig. 1 shows a simplified schematic diagram of a transcutaneous inductive power transmission link, which operates like a transformer. L_1 is the primary coil that is attached to the skin from outside of the body, driven by an ac source V_s, which is often an efficient class-E power amplifier [4]. L_2, is the secondary coil that is implanted under the skin flap along with the rest of the implant electronics. A pair of permanent magnets, one in the center of each coil, can align and hold them together to maximize their mutual inductance *M*. Coil windings have parasitic resistance and capacitance associated with them, which are represented in Fig. 1 by lumped elements R_S, $R_P$and C_P. Capacitors C_{S1} and C_2 are also added to form a pair of resonant LC-tank circuits with L_1 and L_2, respectively, at the power carrier frequency *f*.

So far, these coils have been fabricated with thin wires by using sophisticated winding machinery [5]. However, the need for much smaller footprints in the next generation of high-performance-implantable devices calls for higher geometrical precision and potential for integration on chip or on package. This would require microfabrication techniques that result in lithographically defined planar structures that are known as printed spiral coils (PSCs). PSCs offer more flexibility in defining their characteristics, and have the ability to conform to the body curvature if fabricated on thin flexible substrates, such as polyimide or parylene [6]. Rigid hermetically sealed PSCs can also be fabricated on silicon chips or low-temperature cofired ceramic (LTCC) packages using micromachining (MEMS) technology [7]–[9].

Design and optimization of inductive links with coils made of 1-D filaments have been well studied over the last few decades to find the coil geometries and circuit elements in Fig. 1 that would maximize the amount of power induced in L_2 [5], [10]–[15]. We recently summarized these studies in [16] and combined the theoretical foundation of optimal power transmission in inductive links with simple models that would indicate *M* between a pair of PSCs, their quality factors, and parasitic components. The result was an iterative PSC design methodology that starts with a set of realistic design constraints imposed by the application and PSC fabrication process, and ends with the optimal PSC geometries for maximum power efficiency [16].

For the sake of simplicity, our models in [16] did not include the effects of the PSC surrounding environment. In other words, we only considered the PSC operation in air, which is appropriate for radio-frequency identification (RFID) [17]. However, implantable devices are hermetically sealed in biocompatible materials and surrounded by the conductive tissue underneath the skin. Considering the effects of surroundings in PSC models is imperative in the optimization process because it can affect the PSC parasitic components in Fig. 1 which, in turn, affect the power transfer efficiency.

In this paper, we improve the accuracy of our models in Section II by adding the effects of the PSC coating, substrate, and surrounding environments. We also consider some of the key secondary effects in estimating parasitic components, which play an important role in indicating the PSC quality factor *Q*. In Section III, we utilize the new models in the same iterative optimization method as in [16] by using a combination of closed-form equations in MATLAB (MathWorks, Natik, MA) and verification in finite-element analysis (FEA) tools in HFSS (Ansoft, Pittsburgh, PA). The result is three sets of PSCs, whose geometries are optimized for air, saline, and muscle environments. These PSCs were fabricated on FR4 and characterized in all three environments in Section IV to compare their power transfer efficiency, and validate our PSC models and iterative design procedure.

II. Theoretical Modeling Of Implanted PSCs

The lumped equivalent circuit model of each PSC in Fig. 1 is enclosed in dash-dot boxes. In the following text, we construct a realistic theoretical model for PSCs and discard the numerical subscript wherever we refer to implanted and external PSCs. The lumped parasitic components of the PSC model are influenced by its geometry, material composition, and surrounding environment.

A. Inductance

In this paper, all PSCs are square shaped with rounded corners that have a radius of about a tenth of the side length of the PSC ($d_o/10$) to eliminate sharp edges. Several closed-form equations have been proposed to approximate L in PSCs. We adopted (1) from [18] for square shaped coils

$$L=\frac{1.27\cdot\mu n^2 d_{\mathrm{avg}}}{2}\left[\ln\left(\frac{2.07}{\varphi}\right)+0.18\varphi+0.13\varphi^2\right] \tag{1}$$

where n is the number of turns, $\mu=\mu_0\mu_r$ is permeability, and $d_{\mathrm{avg}} = (d_o+d_i)/2$, where d_o and d_i are the outer and inner side lengths of the coil, respectively. $\varphi = (d_o-d_i)/(d_o+d_i)$ is a parameter known as fill factor, which changes from zero, when all of the turns are concentrated on the perimeter in filament coils, to one, when the turns spiral all the way to the center of the PSC. The accuracy of (1) has an indirect relationship with the s/w ratio, where w and s are the PSC metal line width and spacing, respectively. According to [18], the error in (1) is 8% for s/w = 3 and increases for s/w >3. Moreover, the accuracy of (1) degrades with $\varphi \le 0.1$ or $n \le 2$.

B. Capacitance

Parasitic capacitance C_P is mainly determined by the spacing between planar conductive traces and their surrounding materials. Implantable PSCs are implemented on organic, ceramic, or silicon substrates and coated by an insulator, such as Parylene or silicone. When implanted, they are surrounded by tissue and fluids that have high permittivity, which significantly increase the parasitic capacitance of the PSCs compared to when they are operated in air. To model the unit length parasitic capacitance of an implanted PSC, we can consider it as a coplanar stripline sandwiched between several layers of dielectric substrates, as shown in Fig. 2.

In order to calculate the capacitive coupling between coplanar conductors embedded in a multilayer structure, the effective relative dielectric constant $\varepsilon_{r-\mathrm{eff}}$ of the multilayer structure has to be estimated. It should take into account the effect of all layers and their thicknesses as opposed to only one surrounding material. Conformal mapping is one of the spatial transformation schemes mainly used in the calculation of static 2-D unbounded field problems. Using conformal mapping and superposition of partial capacitances, we have derived the following analytical equations [19]–[21].

Fig. 2 shows the cross section of two traces of the external PSC. The planar metal traces are implemented on a substrate that provides mechanical support and coated on both sides by an insulator. One side of the PSC is air and the other side is the tissue or saline (in some of our measurements). To simplify our analysis, we have considered the tissue only as a single homogeneous layer. To be more realistic, one should discriminate between the skin, fat, muscle, blood, and bone properties [26], [27]. From the conformal mapping technique and superposition of individual layers, the total capacitance per-unit length of the external PSC can be expressed as

$$C_{ext}=\varepsilon_{r-\text{eff}}C_0=C_0+C_{01}+C_{02}+C_{03}+C_{04}+C_{05} \tag{2}$$

where C_0 is the capacitance between adjacent traces in free space and C_{Oi} (i = 1 ~ 5) is the additional partial capacitance of each planar dielectric layer in Fig. 2. Theoretically

$$C_0=\varepsilon_0\frac{K\left(k_0'\right)}{K\left(k_0\right)}, k_0=\frac{2s}{s+2w}, \text{ and } k_0'=\sqrt{1-k_0^2} \tag{3}$$

where $K(k_0)$ is the complete elliptic integral of the first kind [19]. $\varepsilon_{r-\text{eff}}$ of coplanar PSC traces embedded in Fig. 2 multilayer structure can be found from

$$\begin{aligned}\varepsilon_{r-\text{eff}} &=1+\frac{1}{2}\left(\varepsilon_{r1}-1\right)\frac{K(k_0)K\left(k_1'\right)}{K\left(k_0'\right)K(k_1)}+\frac{1}{2}\left(\varepsilon_{r2}-\varepsilon_{r1}\right)\frac{K(k_0)K\left(k_2'\right)}{K\left(k_0'\right)K(k_2)}+\frac{1}{2}\left(\varepsilon_{r3}-1\right)\frac{K(k_0)K\left(k_3'\right)}{K\left(k_0'\right)K(k_3)}+\frac{1}{2}\left(\varepsilon_{r4}-\varepsilon_{r3}\right)\frac{K(k_0)K\left(k_4'\right)}{K\left(k_0'\right)K(k_4)}+\frac{1}{2}\left(\varepsilon_{r5}-\varepsilon_{r4}\right)\frac{K(k_0)K\left(k_5'\right)}{K\left(k_0'\right)K(k_5)}\\ k_i &=\frac{\tanh\left(\frac{\pi s}{4t_i}\right)}{\tanh\left(\frac{\pi(s+2w)}{4t_i}\right)}, k_i'=\sqrt{1-k_i^2}\end{aligned} \tag{4}$$

where ε_{ri} and t_i are the relative dielectric constant and thickness of dielectric layers in Fig. 2, respectively [19]–[21].

Up until this point, we have not yet considered the effect of the PCS metal thickness,t_0, which increases all components of C_{ext} in (2). A good way to include t_0, according to [21], is to adjust the PSC line width and spacing by 2Δ, where

$$\Delta=\frac{t_0}{2\pi\varepsilon_e}\left[1+\ln\left(\frac{8\pi w}{t_0}\right)\right] \tag{5}$$

and ε_e is the mean value of the permittivities of the layers in contact with the strips, as shown in Fig. 3.

In order to access the PSC inner terminal, a conductor should bridge across all other turns of the PSC in a different layer and make a connection to the PSC metal layer through a via. This would result in additional parasitic capacitance between the two overlapping metal layers. The overlapping trace can be considered a microstrip line with the overlapping trace capacitance of

$$C_{\text{ov}}=\varepsilon_0\varepsilon_{r\_\text{eff}\_\text{ov}}\frac{A_{\text{ov}}}{t_{\text{ov}}} \tag{6}$$

where A_{ov} is the overlapping area and T_{ov} is the spacing between the two metal layers, which could be equal to t_5 in Fig. 2 if the substrate has only two metal layers, one on each side.

According to [33], the effective dielectric constant between two conductive plates can be found from

$$\varepsilon_{r\_\,\mathrm{eff}\_\,\mathrm{ov}}=\frac{\varepsilon_{r5}+1}{2}+\frac{\varepsilon_{r5}-1}{2}\left(1+\frac{12}{\frac{w}{t_5}}\right)^{-1/2}-\frac{\varepsilon_r-1}{4.6}\frac{\frac{t_0}{t_5}}{\sqrt{\frac{w}{t_5}}} \tag{7}$$

which includes the fringing effect and thickness of the conductive traces. In our case, since t_5 is relatively large, C_{ov} is less than 2% of the total parasitic capacitance. However, C_{ov} can be significant in integrated or micromachined (MEMS) PSCs, where multiple metal layers are separated by thin dielectric films. Overall, the total parasitic capacitance of the external PSC can be calculated from

$$C_P=C_{\mathrm{ext}}\cdot l_c+C_{\mathrm{ov}} \tag{8}$$

where l_c is the PSC conductor length, found from [16]

$$l_c=4\cdot n\cdot \cdot d_o-4\cdot n\cdot w-(2n+1)^2\,(s+w)\,. \tag{9}$$

For the implanted PSC, we can utilize (2)–(9) with the exception that the dielectric layer 3 (air) should be replaced by the tissue properties, similar to layer 1, depending on the anatomical location of the implanted device.

C. Series Resistance

The series resistance R_S is dominated by the dc resistance of the PSC conductive trace

$$R_{\mathrm{DC}}=\rho_c\frac{l_c}{w\cdot t_0} \tag{10}$$

where ρ_c is the resistivity of the PSC conductive material, which is often a metal with low resistivity, such as gold, platinum, or copper. The skin effect increases the ac resistance of the PSC at high frequencies

$$R_{\mathrm{skin}}=R_{DC}\cdot\frac{t_0}{\delta\cdot(1-e^{-t_0/\delta})}\cdot\frac{1}{1+\frac{t_0}{w}} \tag{11}$$

$$\delta=\sqrt{\frac{\rho_c}{\pi\cdot\mu\cdot f}},\mu=\mu_r\cdot\mu_0 \tag{12}$$

where δ is the skin depth, μ_0 is the permeability of space, and μ_r is the relative permeability of the metal layer [22].

Another effect that contributes to the PSC parasitic resistance is the current crowding caused by the eddy currents, illustrated in Fig. 4. When the magnetic fields of the external PSC or adjacent turns in the same PSC penetrate a planar trace normal to its surface, eddy currents are generated within that trace in a direction that opposes the changes in the magnetic field

NIH-PA Author Manuscript

NIH-PA Author Manuscript

according to Lenz's law. For example, in Fig. 4, the direction of the eddy currents corresponds to an increasing magnetic field. These currents add to the current passing through the inner side of the PSC trace, closest to the center of the spiral, and subtract from the current passing through the outer side. This constriction in the current increases the effective resistance compared to a uniform flow throughout the trace width. The modified resistance by including the effect of eddy currents can be expressed as,

$$R_{\text{eddy}}=\frac{1}{10}R_{\text{DC}}\left(\frac{\omega}{\omega_{\text{crit}}}\right)^2 \tag{13}$$

$$\omega_{\text{crit}}\frac{31.}{\mu_0}\frac{s+w}{w^2}R_{\text{sheet}}. \tag{14}$$

where ω_{crit} is the frequency at which the current crowding begins to become significant and R_{sheet} is the metal trace sheet resistance [23]. Therefore, R_S at the power carrier frequency can be defined as R_{DC} when it is modified by the skin and eddy current effects [24]

$$\begin{aligned} R_S &= R_{\text{skin}}+R_{\text{eddy}} \\ &= R_{\text{DC}}\left(\frac{t_0}{\delta\cdot\left(1-e^{-t_0/\delta}\right)}\cdot\frac{1}{1+\frac{t_0}{w}}+\frac{1}{10}\left(\frac{\omega}{\omega_{\text{crit}}}\right)^2\right). \end{aligned} \tag{15}$$

D. Parallel Resistance

At low RF frequencies, the parallel resistance R_P in the PSC model of Fig. 1 results mainly from the dielectric loss and can reduce the PSC quality factor. Most dielectric materials used in the PSC substrate and coating have small dielectric loss, resulting in very large R_P. In comparison, the tissue is significantly more conductive and its effect should be considered in a multilayer material environment.

We use the partial conductance technique combined with the conformal mapping. Dielectric losses can be described by the loss tangent of each material tan(δ), which is related to its conductivity $\sigma = \varepsilon_0\varepsilon_r\omega \tan(\delta)$. The conformal transformations required for the evaluation of partial conductivities due to different layers are similar to the partial capacitances described in Section II-B [21]. For the external coil, shown in Fig. 2, the equivalent conductance of the PSC unit length is going to be

$$\frac{1}{R_P}=G_P=\frac{\omega\varepsilon_0}{2}\cdot\left[\varepsilon_{r1}\tan\delta_1\frac{K\left(k_1'\right)}{K\left(k_1\right)}+\left(\varepsilon_{r2}\tan\delta_2-\varepsilon_{r1}\tan\delta_1\right)\frac{K\left(k_2'\right)}{K\left(k_2\right)}+\varepsilon_{r3}\tan\delta_3\frac{K\left(k_3'\right)}{K\left(k_3\right)}+\left(\varepsilon_{r4}\tan\delta_4-\varepsilon_{r3}\tan\delta_3\right)\frac{K\left(k_4'\right)}{K\left(k_4\right)}+\left(\varepsilon_{r5}\tan\delta_5-\varepsilon_{r4}\tan\delta_4\right)\frac{K\left(k_5'\right)}{K\left(k_5\right)}\right. \tag{16}$$

where $\tan(\delta_3) = 0$ for air. The same equation can be used for the internal coil equivalent conductance.

E. PSC Quality Factor

From (1)–(16), we can derive all of the parameters needed for calculating the overall impedance and Q of the implanted and external PSCs

$$Z=\frac{R_S+j\omega L}{(R_S+j\omega L)(G_P+j\omega C)+1} \tag{17}$$

$$Q=\frac{\mathrm{Im}(Z)}{\mathrm{Re}(Z)}. \tag{18}$$

From these equations, we can infer that the higher parasitic capacitance resulting from implantation decreases the PSC quality factor, and consequently the power efficiency.

F. Mutual Inductance and Power Transfer Efficiency

A PSC can be considered a set of concentric single-turn loops with shrinking diameters, all connected in series. Therefore, once we find the mutual inductance between a pair of parallel single-turn loops at a certain coupling distance d, the mutual inductance of a pair of PSCs M can be found by summing the partial values between every turn on one PSC and all of the turns on the other PSC [12], [16], [25]. Using M, we can find the PSCs' coupling coefficient, which is the key parameter in power transfer efficiency

$$k=\frac{M}{\sqrt{L_1 L_2}}. \tag{19}$$

It can be shown mathematically that the highest voltage gain and efficiency across an inductive link can be achieved when both LC-tanks are tuned at the power carrier frequency

$$\omega=\omega_0=\frac{1}{\sqrt{L_1 C_{S1}}}=\frac{1}{\sqrt{L_2(C_2+C_{P2})}}. \tag{20}$$

In practice, the secondary PSC is often loaded by the implant electronics R_L as shown in Fig. 1. The loaded secondary quality factor at resonance can be found from [17]

$$Q_L=\left(\frac{R_{S2}}{\omega L_2}+\frac{\omega L_2}{R_L \parallel R_{P2}}\right)^{-1}. \tag{21}$$

The inductive link power transfer efficiency can then be calculated from PSCs' k and quality factors [16]

$$\eta_{12}=\frac{k^2 Q_1 Q_L}{1+k^2 Q_1 Q_L}\cdot\frac{Q_L}{Q_2+Q_L}. \tag{22}$$

It should be noted that most aforementioned parameters in PSCs are interrelated. For example, increasing n in PSCs without changing d_o can increase their L and k. However, it may also decrease Q by increasing R_S due to increased l and reduced ω. Therefore, there are optimal

PSC geometries that would maximize η_{12} as we have previously showed in [16]. Another important parameter is the V_S output resistance, not shown Fig. 1, which is out of the scope of this paper and needs be considered along with the driver's efficiency [4].

III. Optimization of PSCs

A. Optimal Coil

In this section, we use the detailed models built in Section II to design three sets of coils optimized for air, saline, and muscle tissue environments. The material properties of these volume conductors are summarized in Table I [26], [27]. We have adopted the iterative design procedure, described in [16], which starts with a set of design constraints and initial conditions imposed by the PSC application and fabrication process, and ends with the optimal geometries of the PSC pair that maximizes η_{12}.

We have designated the size of the implant to be 10×10 mm^2, which is reasonable for a retinal or cortical visual prosthesis [2], [6]. The nominal coupling distance between the PSCs is considered $d = 10$ mm and the power carrier is set at 13.56 MHz to comply with radio-frequency identification (RFID) standards [17]. However, it could be set to any other band in the 0.1 ~ 50-MHz range, as long as it is well below the PSCs' self resonance frequency (SRF) [28]. We have also used HFSS simulations to verify and fine tune the values suggested by the theoretical model, when they were out of the valid range of our equations (e.g., PSC31).

Table II shows the geometries of the resulting PSCs, specifically optimized for each environment along with the simulation results for Q, k, and η_{12}, when the PSC pair is perfectly aligned. It should be noted that k is the highest in Set-1, resulting in maximum efficiency in the air. However, Q of Set-1 and Set-2 are both smaller than Q of Set-3 in the muscle environment, which results in Set-3 showing the highest efficiency in muscle. Further, it can be seen that for the same implant size and coupling distance, the outer diameter (side length) of the external PSC, shrinks with the increasing dielectric constant and loss tangent.

B. Optimal Coating Thickness

All implantable devices need to be hermetically sealed in a biocompatible material to withstand the harsh environment inside the body without causing an adverse reaction. The receiver coil in inductively powered devices, such as cochlear implants, is often embedded in ceramic, parylene, or medical-grade silicone [1]. The dielectric constant ε_r of silicone coating is much lower than saline or any type of human tissue, as shown in Table I. Therefore, increasing the thickness of the coating will reduce C_P and increase R_P in the PSC model, both of which help increasing Q and, consequentlu, η_{12}. On the other hand, increasing the thickness of the coating will increase d and the volume of the implantable device (tissue displacement), both of which are undesired. Nevertheless, we found it instructive to indicate the optimal coating thickness by sweeping t_{12} in our model (Fig. 2), while maintaining all other parameters constant.

In these model-based simulations, we considered all PSCs in the muscle environment, and maintained the distance between the outer surfaces of the PSC coatings that were facing each other at 10 mm. Also, the thicknesses of the coatings were considered the same for internal and external PSCs. Hence, the actual coupling distance between the two PSC windings was $d = 2t_2 + 10$ mm.

Fig. 5 shows the results of varying the coating thickness of PSCs in Table II. It can be seen from our model that the optimal thickness for Set-3, whose geometries are optimized for the muscle environment, is a reasonable value of t_2 =~ 300 μm. However, the other PSCs need much thicker coatings to reach their maximum efficiencies. This is because their geometries are optimized for lower loss environments and they need thicker coatings to compensate for the additional loss in the muscle environment. Such thicknesses are obviously not realistic for implantable applications.

IV. Simulation and Measurement Results

Fig. 6 shows the PSC measurement setup. We have used a network analyzer (R&S ZVB4) to measure the S-parameters of each coupled PSC pair, while they were mounted vertically at a desired coupling distance using Plexiglas supports. The S-parameters were converted to Z-parameters to calculate k and the quality factors from (17)–(21), which were then substituted in (22) to find find η_{12}[29]. In addition to measurements in air, we used two plastic bags (~ 50 μm thick), hanging from a horizontal clamp, and filled them with saline or beef to emulate implant environments. The internal PSC was sandwiched between the two bags while the external PSC was aligned with it, touching the outer surface of one of the bags (see Fig. 6). The thickness of the layer between PCSs wast_1 = 10 mm, and the layers behind the internal PSCs t_3 were 70 mm and 50 mm for saline and beef, respectively. The saline we used was a solution of distilled water and 9 mg/L NaCl. The beef was bovine sirloin steak, which is the muscle cut from the lower portion of the ribs. The beef temperature at the time of measurement was 10.8 °C and the saline was in equilibrium with the room temperature at 24.0 °C.

A. PSC Quality Factor

In Section III-B, we used our PSC models to find the optimal thickness of the silicone coating on the PSCs in the muscle environment. We coated one sample from each PSC pair in Table II with CF 16–2186 silicone elastomer from NuSil (Carpinteria, CA) up to a thickness of ~ 300 μm. Fig. 7 compares the theoretical calculation, HFSS simulation, and measurement results of PSC21 and PSC31 (both external) quality factors versus carrier frequency, with and without coating, in saline and muscle environments. It can be seen that Q of both PSCs has been improved with the silicone coating as predicted earlier by our model. This improvement is more significant for PSC31, which is coated close to its optimal coating thickness. These curves also show that there is a good agreement among theoretical models, FEA-based simulations (HFSS), and experimental measurement results.

The quality factor of each PSC drops in high permittivity and high conductivity environments, and that leads to higher losses. We evaluated the effects of geometry optimizations in Section III-A on the Q of PSCs in each environment. Fig. 8 shows how the Q of coated PSC11 and PSC31 change versus frequency in the air and muscle environments. PSC11 is optimized for air. Therefore, at 13.56 MHz, its Q decreases by 78% from 128 in air to 28 in the muscle environment due to changes in C_P and R_P, which also result in significant reduction in PSC11's SRF. On the other hand, the Q of PSC31 decreases only by 25% from 122 in air to 92 in muscle. The agreement among calculation, simulation, and measurement results in Fig. 8 demonstrates the efficacy of the geometrical optimization algorithm and models described in Section II, which have helped to improve the PSC quality factors by a factor of ~3.3 in the muscle environment.

Optimization of the implanted PSC for the surrounding environment is influenced by the dramatic changes in the geometry of the external PSC. A comparison between PSC12 and PSC32 in Table II shows that optimization for the muscle environment has reduced n_{32} and w_{32}, both of which reduce C_{P2} and R_{P2}. In measurements, Q of PSC12 and PSC32 is reduced from 51.5 and 36.6 in the air to 42.3 and 36 in the muscle environment, respectively. Even though the optimized PSC12 offers a slightly higher Q than PSC32, it has a weaker coupling to PSC31. This is mainly due to the size constraint applied to the implanted PSC (10 × 10 mm^2). Therefore, the resulting power transfer efficiency in muscle for Set-3 is higher than Set-1, as discussed in Section IV-B.

B. Power Transfer Efficiency

PSC pair geometries affect k and Q, both of which are key factors in η_{12} according to (22). Here, we compare the power transfer efficiency of the three sets of PSCs in Table II in the air, saline, and muscle environments, in Fig. 9(a)–(c), respectively, through model-based theoretical calculations, FEA simulations, and experimental measurements. The PSCs are perfectly aligned and their coupling distance on the horizontal axis includes their coating thickness (300 μm). The carrier frequency is held constant at 13.56 MHz, and the secondary PSC is loaded with R_L = 500 Ω.

Fig. 9 curves show that each set of PSCs performs best in its designated operating environment, most important of which is the muscle, where an implantable device eventually resides. Fig. 9 (c) obviously shows that a pair of PSCs that is optimized for air (Set-1) provides the worst η_{12} when implanted in the muscular tissue. While Set-1 PSC pair can achieve more than 70% efficiency in the air due to their high k, their η_{12} drops to only 21.8% in the muscle environment due to degradation in their Q, as seen in Fig. 8(a). The Set-3 pair, on the other hand, provides η_{12} >30% at d = 10 mm due to PSC31 smaller geometries, which is optimized for this environment. These results signify the importance of using detailed models in designing implantable PSCs, in which the effects of parasitic components have been taken into account.

Fig. 9 also shows reasonable agreement among theoretical calculations from our models, finite-element simulations, and measurement results. There are, however, small discrepancies due to the following reasons, some of which are related to our models and some are related to the measurement setup: 1) inherent limitations in the accuracy of the closed-form equations, particularly when the PSC parameters are close to or out of their valid range of parameters; 2) large line width and small number of turns, resulting from our optimization algorithm particularly for Set-3 (Table II), causing the shape of PSC13 to deviate from a perfect square with rounded corners, affecting the validity of (1); 3) secondary effects, such as fringing and capacitive coupling between the two inductively coupled PSCs, which were not included in our models; 4) manually applied silicone coating was not quite uniformly distributed on the PSC surfaces; 5) there could be small patches of air gap between the plastic bags containing the volume conductors and the outer surface of the PSCs' silicone coating; and 6) the 50-μm-thick plastic bag, made of polyethylene (PE) with ε_r = 2.3 and tan(δ) = 0.0002, which was considered to be part of the PSC silicone coating.

V. Conclusion

We have constructed detailed models and devised design paradigms for small PSCs that are meant to be fabricated on rigid or flexible planar substrates, coated with biocompatible dielectric materials, such as silicone, and implanted in homogeneous tissue environments. Various phenomena that could result in degradation of the PSC quality factors, due to coating and implantation, were considered in our models. We combined our models with an iterative PSC design procedure, previously reported in [16], to optimize the PSC geometries for providing maximum power transfer efficiency in tissue environments. This can result in lower heat dissipation, extended battery lifetime, and improved safety in neuroprosthetic devices, such as retinal or cortical implants, with demanding size constraints [30].

We validated the PSC design procedure by applying it to an exemplar 1-cm^2 implantable visual prosthesis operating at 13.56 MHz. We constructed finite-element analysis models in HFSS using the resulting optimal geometries and simulated them. We also fabricated several PSC pairs on FR4 and conducted experimental measurements in air, saline, and muscle environments. All calculation, simulation, and measurement results were in close agreement within the desired range of design parameters, and demonstrated the validity of the models and proposed iterative PSC design procedure. We are now utilizing the proposed method in the design and development of a multicarrier inductive wireless link for high-performance neuroprosthetic devices [31], [32]. We plan to fabricate the optimized PSCs on higher quality substrates with smaller feature size using microelectromechanical system (MEMS) technology.

Acknowledgments

The authors would like to thank members of the GT-Bionics lab for their help with the measurements.

This work was supported in part by the National Institute of Health grant 1R01NS062031-01A1, and in part by the National Science Foundation under Award ECCS-824199.

Biographies

Uei-Ming Jow (S'07) received the B.E. degree in electrical engineering from Tatung University, Taipei, Taiwan, in 1999, the M.S. degree in electronic engineering from the National Taiwan University of Science and Technology, in 2001, and is currently pursuing the Ph.D. degree in electrical and computer engineering at the Georgia Institute of Technology, Atlanta.

From 2001 to 2006, he joined the Industrial Technology Research Institute, Hsinchu, Taiwan, and was an RF Engineer in the Electronics Research and Service Organization. He was involved in the analysis of electromagnetic compatibility for the high-speed digital circuit as well as the embedded RF circuit packaging technology. His main research interests are neural engineering, bionic systems, integrated analog circuit design, and wireless-implantable biomedical systems.

NIH-PA Author Manuscript

NIH-PA Author Manuscript

Maysam Ghovanloo (S'00–M'04) was born in Tehran, Iran, in 1973. He received the B.S. degree in electrical engineering from the University of Tehran, Tehran, Iran, in 1994, the M.S. degree in biomedical engineering from the Amirkabir University of Technology, Tehran, in 1997, and the M.S. and Ph.D. degrees in electrical engineering from the University of Michigan, Ann Arbor, in 2003 and 2004, respectively.

From 2004 to 2007, he was an Assistant Professor in the Department of Electrical and Computer Engineering at North Carolina State University, Raleigh. In 2007, he joined the faculty of Georgia Institute of Technology, Atlanta, where he is currently an Assistant Professor and the Founding Director of the Georgia Tech Bionics Laboratory in the School of Electrical and Computer Engineering. He has authored or coauthored many conference and journal publications.

Dr. Ghovanloo is an Associate Editor of the IEEE Transactions on Circuits and Systems, Part II. He received awards in the 40th and 41st Design Automation Conference (DAC)/International Solid-State Circuits Conference (ISSCC) Student Design Contest in 2003 and 2004, respectively. He has organized special sessions and was a member of Technical Review Committees for several major conferences in the areas of circuits, systems, sensors, and biomedical engineering. He is a member of the Tau Beta Pi, the Sigma Xi, and the IEEE Solid-State Circuits Society, the IEEE Circuits and Systems Society, and the IEEE Engineering in Medicine and Biology Society.

References

[1]. Cochlear Corp.. Nucleus freedom implant. [Online]. Available: http:// www.cochlearamericas.com/Products/23.asp

[2]. Humayun MS, Weiland JD, Fujii GY, Greenberg R, Williamson R, Little J, Mech B, Cimmarusti V, Boemel GV, Dagnelie G, de Juan E Jr. Visual perception in a blind subject with a chronic microelectronic retinal prosthesis. Vis. Res Nov;2003 43:2573–2581. [PubMed: 13129543]

[3]. Harrison RR, Watkins PT, Kier RJ, Lovejoy RO, Black DJ, Greger B, Solzbacher F. Wireless neural recording with single low-power integrated circuit. IEEE Trans. Neural Syst. Rehab. Eng. to be published.

[4]. sokal NO, Sokal AD. Class-E-A new class of high-efficiency tuned single-ended switching power amplifiers. IEEE J. Solid-State Circuits Jun;1975 SSC-10(no. 3):168–176.

[5]. Yang Z, Liu W, Basham E. Inductor modeling in wireless links for implantable electronics. IEEE Trans. Magn Oct;2007 43(no. 10):3851–3860.

[6]. Shah MR, Phillips RP, Normann RA. A study of printed spiral coils for neuroprosthetic transcranial telemetry applications. IEEE Trans. Biomed. Eng Jul;1998 45(no. 7):867–876. [PubMed: 9644895]

[7]. Von Arx JA, Najafi K. A wireless single-chip telemetry-powered neural stimulation system. Proc. IEEE Intl. Solid-State Circuits Conf. Digest Feb;1999 :214–215.

[8]. Töpper M, Klein M, Buschick K, Glaw V, Orth K, Ehrmann O, Hutter M, Oppermann H, Becker KF, Braun T, Ebling F, Reichi H, Kim S, Tathireddy P, Chakravarty S, Solzbacher F. Biocompatible hybrid flip chip microsystem integration for next generation wireless neural interfaces. Proc. IEEE Elect. Components Tech. Conf May;2006 :705–708.

[9]. Kim S, Zoschke K, Klein M, Black D, Buschick K, Toepper M, Tathireddy P, Harrison R, Oppermann H, Solzbacher F. Switchable polymer-based thin film coils as a power module for wireless neural interfaces. Sens. Actuators A Nov;2007 136:467–474.

[10]. Ko WH, Liang SP, Fung CDF. Design of radio-frequency powered coils for implant instruments. Med. Biol. Eng. Comput 1977;15:634–640. [PubMed: 203785]

[11]. Heetderks WJ. RF powering of millimeter and submillimeter-sized neural prosthetic implants. IEEE Trans. Biomed. Eng May;1988 35(no. 5):323–327. [PubMed: 3397079]

[12]. Zierhofer CM, Hochmair ES. Geometric approach for coupling enhancement of magnetically coupled coils. IEEE Trans. Biomed. Eng Jul;1996 43(no. 7):708–714. [PubMed: 9216142]

[13]. Neagu CR, Jansen HV, Smith A, Gardeniers JGE, Elwanspoek M. Characterization of a planar microcoil for implantable microsystems. Sens. Actuators A 1997;62:599–611.

[14]. Kendir GA, Liu W, Wang G, Sivaprakasam M, Bashirullah R, Humayun MS, Weiland JD. An optimal design methodology for inductive power link with class-E amplifier. IEEE Trans. Circuits Syst. I May;2005 52(no. 5):857–866.

[15]. Baker MW, Sarpeshkar R. Feedback analysis and design of RF power links for low-power bionic systems. IEEE Trans. Biomed. Circuits Syst Mar;2007 1(no. 1):28–38.

[16]. Jow U, Ghovanloo M. Design and optimization of printed spiral coils for efficient transcutaneous inductive power transmission. IEEE Trans. Biomed. Circuits Syst Sep;2007 1(no. 3):193–202.

[17]. Finkenzeller, K. RFID Handbook: Fundamentals and Applications in Contactless Smart Cards and Identification. 2nd ed.. Wiley; Hoboken, NJ: 2003.

[18]. Mohan SS, del Mar Hershenson M, Boyd SP, Lee TH. Simple accurate expressions for planar spiral inductances. IEEE J. Solid-State Circuits Oct;1999 34(no. 10):1419–1424.

[19]. Pieters P, Vaesen K, Brebels S, Mahmoud SF, DeRaedt W, Beyne E, Mertens RP. Accurate modeling of high-Q spiral inductors in thin-film multilayer technology for wireless telecommunication applications. IEEE Trans. Microw. Theory Tech Apr;2001 49(no. 4, pt. 1):589–599.

[20]. Hoffmann, RK. Handbook of Microwave Integrated Circuit. Artech House; Norwood, MA: 1987.

[21]. Gevorgian S, Berg H, Jacobsson H, Lewin T. Basic parameters of coplanar-strip waveguides on multilayer dielectric/semiconductor substrates, Part 1: High permittivity superstrates. IEEE Microw. Mag Jun;2003 4(no. 2):60–70.

[22]. Wheeler HA. Formulas for the skin effect. Proc. IRE Sep;1942 30,(no. 9):412–424.

[23]. Kuhn WB, Ibrahim NM. Analysis of current crowding effects in multiturn spiral inductors. IEEE Trans. Microw. Theory Tech Jan;2001 49(no. 1):31–38.

[24]. Ulrich, RK.; Schaper, LW. Integrated Passive Component Technology. Wiley; Hoboken, NJ: 2003. ch. 11.

[25]. Akyel C, Babic S, Kincic S. New and fast procedures for calculating the mutual inductance of coaxial circular coils (circular coil-disk coil). IEEE Trans. Magn Sep;2002 38(no. 5):2367–2369.

[26]. Gabriel S, Lau RW, Gabriel C. The dielectric properties of biological tissues: II. Measurements in the frequency range 10 Hz to 20 GHz. Phys. Med. Biol Nov;1996 41:2251–2269. [PubMed: 8938025]

[27]. Kim J, Oh D, Yoon J, Cho S, Kim N, Cho J, Kwon Y, Cheon C, Kim Y. In vitro and in vivo measurement for biological applications using micromachined probe. IEEE Trans. Microw. Theory Tech Nov;2005 53(no. 11):3415–3421.

[28]. Jow U, Ghovanloo M. Optimization of a multiband wireless link for neuroprosthetic implantable devices. Proc. IEEE Biomed. Circuits Syst Nov;2008 :97–100.

[29]. Pozar, DM. Microw. Eng. Wiley; New York: 1998. ch. 4.

[30]. Lazzi G. Thermal effects of bioimplants. Proc. IEEE Eng. Med. Biol. Mag Sep;2005 24(no. 5):75–81.

[31]. Ghovanloo, M.; Lazzi, G. Transcutaneous magnetic coupling of power and data. In: Akay, M., editor. Wiley Encyclopedia of Biomedical Engineering. Wiley; Hoboken, NJ: 2006.

[32]. Ghovanloo M, Atluri S. A wideband power-efficient inductive wireless link for implantable microelectronic devices using multiple carriers. IEEE Trans. Circuits Syst. I, Reg. Papers Oct;2007 54(no. 10):2211–2221.

[33]. Bahl IJ, Garg R. Simple and accurate formulas for a microstrip with finite strip thickness. Proc. IEEE Nov;1977 65(no. 11):1611–1612.

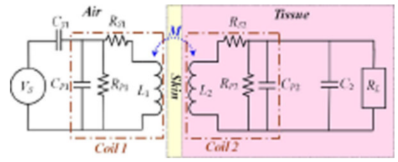

Fig. 1.
Simplified schematic diagram of the inductive link with lumped equivalent circuit components.

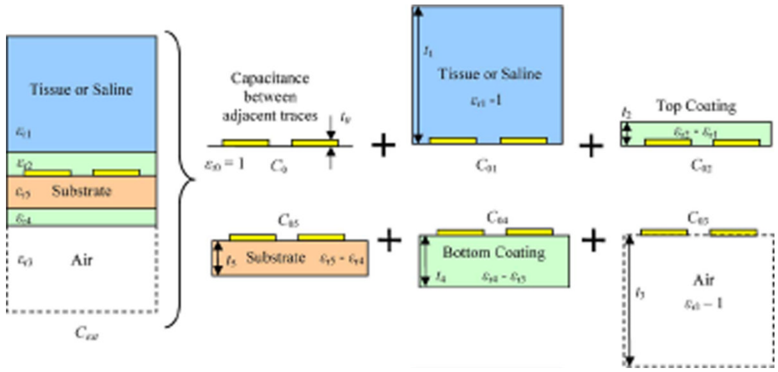

Fig. 2.
Modeling of the parasitic capacitance created by the multilayer material surrounding the external PSC [19].

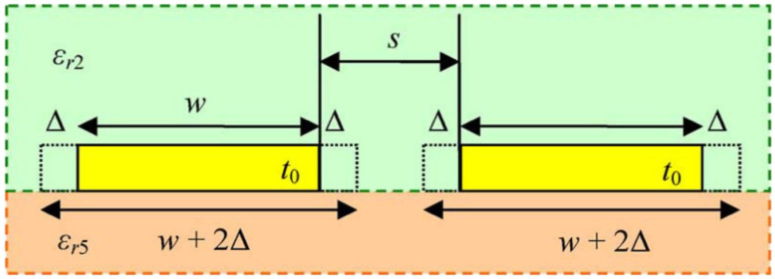

Fig. 3.
Modification of the PSC line width and spacing to account for the metal thickness t_0 [21].

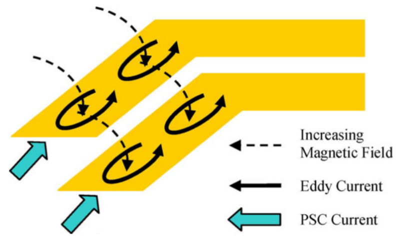

Fig. 4.
Demonstration of the current crowding effect [23].

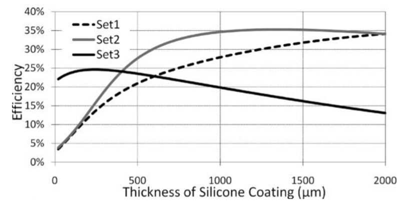

Fig. 5.

Optimal thickness of the silicone coating on both sides of each PSC with geometries given in Table II in the muscle environment. The distance between the coating surfaces that face each other is fixed at 10 mm.

NIH-PA Author Manuscript

NIH-PA Author Manuscript

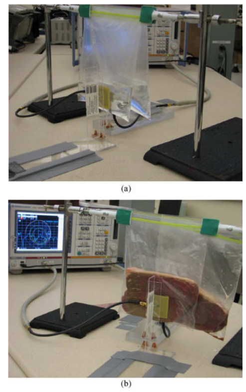

Fig. 6.
Experimental setup for measuring inductive link properties between a pair of PSCs in the air, saline (a), and muscle (b) environments.

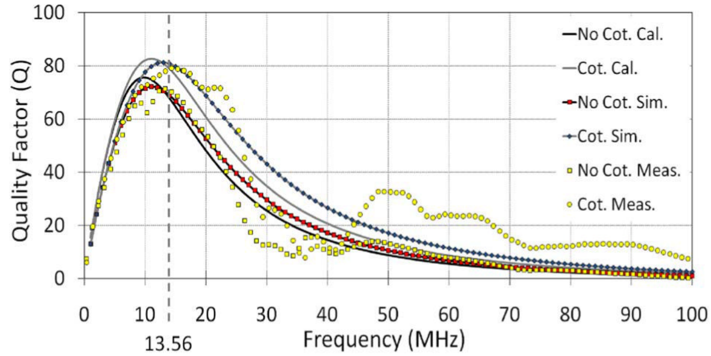

(a)

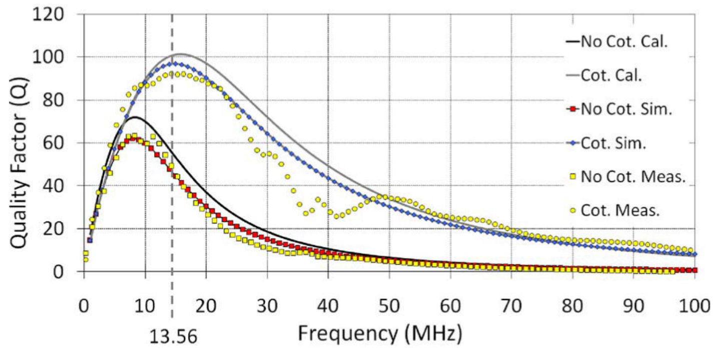

(b)

Fig. 7.

Comparison between theoretical calculations, HFSS simulations, and measurement results of *Q* variations versus carrier frequency of (a) PSC21 in saline and (b) PSC31 in muscle, with and without 300-μm silicone coating.

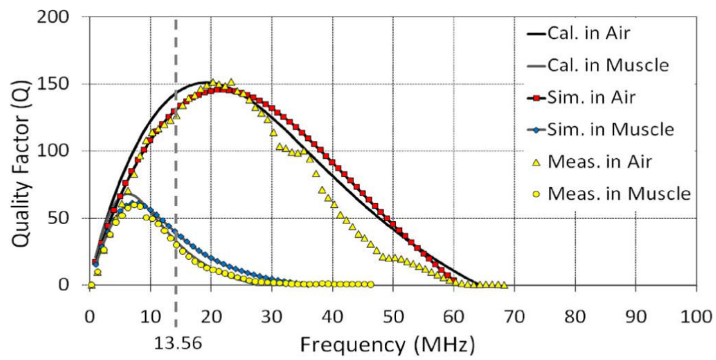

(a)

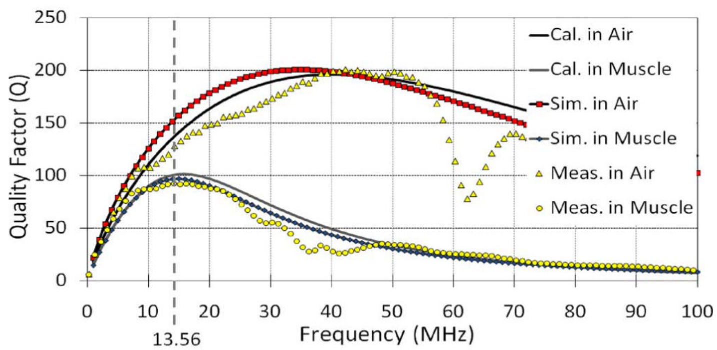

(b)

Fig. 8.

Comparison between theoretical calculations, HFSS simulations, and measurement results of *Q* variations versus carrier frequency in (a) PSC11 that is optimized for air, and (b) PSC31 that is optimized for muscle, in these two environments (see Table II for PSC geometries).

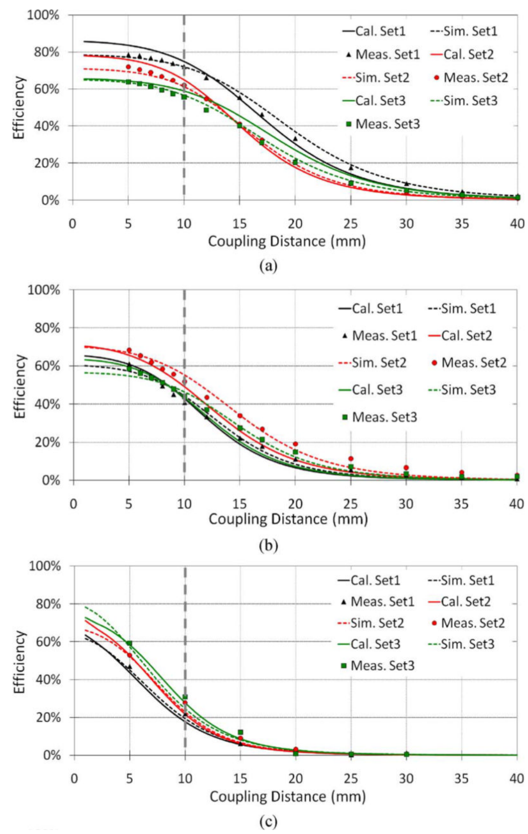

Fig. 9.

Variations of the power transfer efficiency with coupling distance at 13.56 MHz for three sets of PSCs in Table II optimized for (a) air, (b) saline, and (c) muscle environments.

TABLE I

Material Properties

Material	Air	Saline	Muscle	FR4	Silicone
f[MHz]	13.56	13.56	13.56	13.56	13.56
σ [S/m]	0	0.60	0.58	1.33e−4	2.26e−6
ε_r	1	78	136	4.4	3.0
tan(δ)	0	10.2	6.0	0.04	0.001

*Derived from [26] and [27].

TABLE II

Optimized PSC Geometries and Inductive Link Characteristics From Simulation Results

Parameter	Set-1		Set-2		Set-3	
Material	Air		Saline		Muscle	
Name	PSC11	PSC12	PSC21	PSC22	PSC31	PSC32
d_o (mm)	38	10	30	10	24	10
di (mm)	14.9	5.8	11.1	5.5	9.4	7.2
φ	0.44	0.27	0.46	0.29	0.46	0.16
n (turns)	7	6	3	5	2	4
w (μm)	1500	200	3000	250	3500	150
s (μm)	150	150	150	150	150	150
L (μH)	1.66	0.51	0.26	0.33	0.12	0.34
R_s (Ω)	0.93	0.72	0.22	0.44	0.06	0.72
R_P (kΩ)	758	3120	7.19	18.34	2.36	1.68
C_P (pF)	3.12	0.18	7.88	1.37	7.72	0.77
C_{s1} / C_2 (pF)	83.0	270.1	510.2	417.5	1148	450
SRF (MHz)	70	525	122	236	165	302
Q	128	60	81	55	96	32
k	0.0697		0.0518		0.0301	
η_{12_cal} (%)♦	72.05		55.22		29.85	
η_{12_sim} (%)	74.86		49.12		27.70	
η_{12_meas} (%)♠	72.22		51.80		30.84	

*For perfectly aligned PSCs with a nominal coupling distance of d 10 mm at f = 13.56 MHz and R_L = 500 Ω, coated with a 300 μm layer of silicone.

♦Calculation results.

♠Measurement results.